Structure and Dynamics of M13mp19 Circular Single-Strand DNA: Effects of Ionic Strength

DAVID H. WILSON, HARRY L. PRICE, JEFF HENDERSON, SUE HANLON and ALBERT S. BENIGHT*

Department of Chemistry and Department of Biological Chemistry, University of Illinois at Chicago, Chicago, Illinois 60680

SYNOPSIS

Dynamic and static light scattering, CD, and optical melting experiments have been conducted on M13mp19 viral circular single-strand DNA as a function of NaCl concentration. Over the 10,000-fold range in concentration from 100 μM to 1.0M NaCl, the melting curves and CD spectra indicate an increase in base stacking and stability of stacked regions with increased salt concentration. Analysis of dynamic light scattering measurements of the single-strand DNA solutions as a function of K^2 from 1.56 to 20×10^{10} cm^{-2} indicates the collected autocorrelation functions are biexponential, thus revealing the presence of two decaying dynamic components. These components are taken to correspond to (1) global translational motions of the molecular center of mass and (2) motions of the internal molecular subunits. From the evaluated relaxation rates of these components, diffusion coefficients D_0 and D_{plat} are determined. The center of mass translational diffusion coefficient D_0, varies in a nonmonotonic manner, by 10%, from 3.75×10^{-8} to 3.39×10^{-8} cm^2/s over the NaCl concentration range from 100 μM to 1.0M. Likewise, the radius of gyration R_G, obtained from static light scattering experiments, varies by 15% from 699 to 830 Å over the same NaCl range. D_{plat}, the diffusion coefficient of the internal subunits, displays a different dependence on the NaCl concentration and decreases, by nearly 22% in a titratable fashion, from 12.46×10^{-8} to 10.26×10^{-8} cm^2/s, when the salt is increased from 100 μM to 1.0M. A semiquantitative interpretation of these results is provided by analysis of the light scattering data in terms of the circular Rouse–Zimm chain. Rouse–Zimm model parameters are estimated from the experimental results, assuming the circular chains are composed of a fixed number of Gaussian segments, $N + 1 = 15$. The rms displacement of the internal segments, b, is estimated to be the smallest (442 Å) in 100 mM NaCl. Increases of b to 467 Å in 100 μM and 524 Å in 1.0M NaCl are observed. Meanwhile, the hypothetical friction factor of the internal subunits, f, progressively increases as the NaCl concentration is raised. It is inferred from the evaluated Rouse–Zimm model parameters that both the static flexibility of the circular chain and diffusive displacements of the internal subunits decrease with increases in NaCl concentration from 100 mM to 1.0M. These decreases directly contrast the salt-dependent behavior of double-stranded DNA, where greater flexibility is observed when the Na^+ concentration is increased. The melting and CD measurements indicate the decrease in flexibility and internal motions is due to the formation of nucleotide stacking in the higher NaCl environments. In 100 μM NaCl, where stacking is highly unfavored, a significant electrostatic contribution to the persistence length likely acts to stiffen the molecule. It appears the observable changes in the internal dynamics of M13mp19 single-strand DNA are associated with increases in base stacking that occur from 100 μM to 1.0M NaCl, which apparently induce relatively small perturbations in the overall global tertiary conformation of the DNA.

CCC 0006-3525/90/020357-20 $04.00

Biopolymers, Vol. 29, 357–376 (1990)

*To whom all correspondence should be addressed.

INTRODUCTION

Interactions between single-strand DNA (ssDNA) and regulatory proteins that preferentially bind ssDNA over duplex double-stranded DNA are intrinsic to many processes involved in genetic control.[1,2] Biological processes such as DNA replication,[3,4] recombination,[5-7] and repair[8] are directly influenced by complex formation of single-strand specific proteins with ssDNA. Consequently, the biochemical and physical properties of a number of proteins that specifically bind ssDNA have been the focus of intense study.[9-15] A recently reported comparison of the amino acid sequences of five well-known ssDNA binding proteins revealed a common sequence (and possible structural) motif among the proteins.[16] Sequence alignment of aromatic and charged residues revealed common domains in all the proteins. This observation, although not conclusive, supports the presently prevailing notion that two of the major stabilizing forces of protein/ssDNA complexes are (1) stacking interactions between the DNA bases and aromatic residues[17] of the protein and (2) electrostatic interactions between the basic peptide residues and negatively charged phosphate backbone of the ssDNA.[18] If this is the case, stable complex formation necessarily depends on local conformations of both the protein and ssDNA molecules comprising the complex. Therefore, a necessary first step to unraveling factors involved in ssDNA/protein interactions requires an understanding of the local structures and dynamics of the ssDNA alone.

Previous reports of hydrodynamic,[19-22] electron micrographic,[19,23] chemical cross-linking,[24,25] restriction enzymatic,[26] and DNA polymerase mapping studies of ssDNA[27] have been published. The ssDNAs studied were either precursors of the same ssDNA studied here, M13mp19, or similar DNAs from prokaryotic bacteriophages fd or ΦX174. From these studies it has become clearly evident that circular ssDNA can adopt a manifold of intramolecular secondary structures. Among these are small hairpins or stem-loop structures containing from approximately 30 to 300 base pairs that form on palindromic or partially self-complementary regions proximal to each other.[23] Long-range structures comprised of much larger hairpins nucleated by self-complementary sequences separated by several thousand nucleotides have also been observed in electron micrographs.[23,24] Regions of single-strand viral DNA containing appreciable amounts of both short- and long-range hairpin loops have been implicated as a means by which single-strand specific proteins are directed to interact with specific single-strand regions or induced into different modes of binding.[13,28-30] Restriction enzyme digestion analysis of single-strand ΦX174 and M13 DNA indicated specific sequence duplex regions form in the single-strand DNAs that are recognized and cleaved by double-strand sequence-specific restriction enzymes.[26] Recently published studies on model synthetic oligomers have demonstrated the potential for formation of parallel-stranded DNA.[31-33] Thus the possibility for directly symmetric sequences to form secondary structures also exists in ssDNA.

In this paper, results of dynamic and static light scattering, thermal denaturation and CD experiments on M13mp19 circular ssDNA as a function of NaCl concentration from 100 μM to 1.0M NaCl are reported. The melting curves and CD spectra are consistent with the reports mentioned above of other ssDNAs and indicate M13mp19 ssDNA also contains considerable secondary structure. Static light scattering measurements provide a measurement of the hydrodynamic dimensions via the radius of gyration R_G of the ssDNA molecules in solution, and how these depend on NaCl concentration. Dynamic light scattering measurements conducted in the near uv (351.1 nm) over a wide range of scattering angles θ ($30° < \theta < 140°$) provide an evaluation of the center of mass diffusion coefficient D_0 as a function of NaCl concentration. In addition, a diffusion coefficient related to the motions of the internal molecular subunits D_{plat}, is evaluated at each NaCl concentration. Semiquantitative interpretations of the light scattering results are made in terms of the Rouse–Zimm circular Gaussian chain.[34-37]

Results of our investigations indicate the following: (1) Translational motions of the ssDNA center of mass are isotropic and change only slightly as NaCl concentration is increased over a 10,000-fold range from 100 μM to 1.0M. (2) The static flexibility, which is inversely proportional to the persistence length of the circular DNA chains, appears to decrease with increases in NaCl concentration above 100 mM and then decrease when the salt is lowered from 100 mM to 100 μM. (3) Motions of the internal subunits, which act to relax short wavelength fluctuations ($\leq$ 250 Å), decrease progressively with increasing NaCl over the entire salt range. Since the amount of nucleotide stacking increases with increasing NaCl concentration, it is surmised the decrease in the diffusive displace-

ments of the internal subunits is due to restrictions imposed on them by the formation of stacking interactions along the ssDNA.

MATERIALS AND METHODS

Cell Growth and DNA Isolation

Single-strand, closed circular M13mp19 phage DNA[38] was isolated from a single preparation of infected *Escherichia* coli strain JM101 (New England Biolabs, Beverly, MA). Uninfected JM101 cells were made competent by the standard $CaCl_2$ treatment[39] and transformed with double-stranded M13mp19 RFI DNA (New England Biolabs). Since M13mp19 RFI DNA contains the Lac Z gene, successful transformants produced blue plaques when the transformation mixture was plated on M9 minimal media agar containing X-GAL (5-Bromo-4-chloro-3-indolyl-β-D-galactopyranoside, Boehringer-Mannheim, Indianapolis, IN) and incubated at 37°C for 24 h.[40] Ten milliliters of M9 minimal media were inoculated with a single blue plaque and cell growth continued with shaking for 6 h at 37°C. Twenty liters of M9 media were then inoculated with this 10-mL preculture and the culture was grown for ~ 26 h at 37°C under forced aeration and agitation.

Viral DNA was isolated by published procedures.[41] The uv absorbance spectrum of the purified M13mp19 single-strand DNA indicated an absorbance ratio of $A_{260}/A_{280} = 1.8$–1.9. Homogeneity and purity of the isolated sample was verified by electrophoresis on native and alkaline agarose gels. In native agarose gels (0.8–1.2%) the isolated M13mp19 sample migrated the same distance as a previously characterized single-strand M13mp19 DNA standard. Electrophoresis on alkaline denaturing gels (1.4% agarose, 30 m*M* NaOH)[42] demonstrated that less than 2% of the total purified DNA was in the linear form. From a single 20-L preparation, 10 mg of purified M13mp19 ssDNA was obtained. A second M13mp19 viral DNA sample was isolated and purified by identical procedures six months later and used to verify the reproducibility of a representative portion of the data obtained on the first DNA sample.

The extinction coefficient used to determine concentrations of our M13mp19 samples was determined according to the method of Pohl and Jovin.[43] P1 nuclease and 5′-deoxymononucleotides were purchased from Sigma (St. Louis, MO). By digesting the DNA to completion with P1 and performing a linear regression of the digested spectra against the four 5′-deoxymononucleotide reference spectra (Henderson, Benight, Miabenco, and Hanlon, unpublished) an extinction coefficient, $\epsilon_{260} = 8460 M^{-1} \cdot cm^{-1}$, was evaluated.

Preparation of DNA Samples

DNA samples were prepared for dynamic and static light scattering measurements by dilution in the appropriate buffered salt solution to a concentration of ~ 1.0 optical density (OD)/mL (118 μM nucleotides) as determined by the absorbance at 260 nm. The buffer solution was 10 m*M* Tris HCl, 1 m*M* EDTA, pH = 7.5, containing 1.0*M*, 500 m*M*, 100 m*M*, or 100 μM NaCl. Sodium ion concentrations were independently verified by measured conductivity values on the four DNA solutions. Samples were gently filtered under slight syringe pressure through 0.45-μm pore polysulphone filters (Gelman Sciences, Ann Arbor, MI) into a cylindrical scattering cell that had been prewashed with filtered water and the appropriate filtered buffered NaCl solution. Samples were routinely refiltered (at least twice) until large dust particles, which produced obvious scattering "Tyndalls," seen when the scattering cell illuminated with 632.8 nm laser light was viewed at low angles, were removed. The total volume of each sample was ~ 6–10 mL.

For melting curve measurements the same samples used for the dynamic light scattering measurements were diluted with the appropriate solvent to a concentration of ~ 0.35 OD/mL (41 μM nucleotides) and stored at 4°C. Prior to melting, 1.5 mL of the sample and solvent reference solution were placed in 1-cm path-length quartz cuvettes, degassed by bubbling with prepurified helium, and tightly sealed with teflon stoppers. Before collection of melting curve data, the sample and reference were equilibrated at the starting temperature (10°C) for 1 h.

Samples for the CD measurements were prepared from the same samples used in the dynamic and static light scattering measurements. Prior to CD measurements all the material remaining from the dynamic light scattering samples was pooled, divided into four equal volumes, and exhaustively dialyzed vs the same buffer and four NaCl concentrations as previously described, except the buffer pH was 7.9 instead of 7.5. This slightly higher buffer pH is not expected to greatly influence the

CD measurements or alter comparison of the results from them with the other experiments. DNA concentrations were ~ 0.4 OD/mL (47 μM nucleotides) as determined from the absorbance at 260 nm and the evaluated extinction coefficient. CD spectra were reduced to mean residue ellipticity with units of deg · cm^2/decimole nucleotide.

Dynamic Light Scattering (DLS) Measurements

All DLS experiments were performed at 20°C. The light source for the DLS measurements was a Coherent Innova 90-6 Argon ion laser operating at a wavelength of 3511 Å and a single line power of ~ 150 mW. Single mode operation in the transverse TEM_{00} mode was optimized by an intracavity etalon and aperture. The multiangle goniometer allowed data collection at scattering angles from 30° to 140°. The 3511 Å wavelength and angular range provided access of K^2, the square of the scattering vector, from 1.5 to 20.5 × 10^{10} cm^{-2}. The scattering vector is defined as $K = (4\pi n/\lambda_0)\sin(\theta/2)$, where n is the refractive index of the solvent, λ_0 is the incident light wavelength in vacuo, and θ is the scattering angle.[44] Definition of the scattering volume and detection optics were, with slight modifications, patterned after the optical configuration described by Thomas and Schurr.[45] The scattering cell is fused silica and cylindrical, 2.9 cm in diameter with flat 4-mm wide parallel faces for normal entrance and exit of the laser beam. The parallel faces of the cell are separated by 2.8 cm and the cell wall thickness is 1.6 mm. Photons scattered at the detector were collected by a Thorn-EMI (Fairfield, NJ) 9863B/350 photomultiplier tube. Photomultiplier current pulses were sent through an amplifier-discriminator (model AD6, Pacific Instruments, Inc, Concord, CA), converted to a TTL pulse train (pulse width = 10 ns), and passed to a digital correlator (Langley-Ford model 1096, Coulter Electronics, Hialeah, FL) with 272 correlator channels available for autocorrelation of the pulses. Collected autocorrelation functions were passed to an IBM-AT personal computer for analysis.

Prior to our experiments on M13mp19 ssDNA, we performed a series of rigorous control experiments with monodisperse and binary mixtures of polystyrene spheres. These control experiments served not only to verify optical and angular alignment of the spectrometer, they also established the optimum level of sensitivity capable of our experimental apparatus.

Static Light Scattering Measurements

All static intensity measurements were recorded at 20°C. Measurements were made with a Brice-Phoenix light scattering photometer (C. N. Wood Manufacturing Co., New Town, PA). The light source (a high-pressure mercury vapor lamp) provided unpolarized incident light at a wavelength of 436 nm. Ratios of the intensity of light scattered at a particular angle θ, i_θ, to the total incident intensity I_0, (i_θ/I_0) were measured every 5° from 30° to 70°. Intensity readings were determined from galvanometer readings of the phototube detector. From i_θ/I_0 values and instrumental constants of the system the Rayleigh ratio R_θ was determined at each angle in the standard way.[46] Determination of the optical constant κ for the scattering photometer was previously described.[47] Plots of κ/R_θ vs $\sin^2(\theta/2)$ were linear at all NaCl concentrations. From the slopes and y intercepts of the linear equations determined by a least-squares fit to the data points, R_G, the radius of gyration of the ssDNA in each salt environment was evaluated.[48] Cross calibration of the static light scattering photometer with the dynamic light scattering spectrometer was done with a clean monodisperse preparation of polystyrene latex spheres of known hydrodynamic radius (300 or 450 Å). The spherical radius measured by either instrument agreed within 1 Å and agreed within 5 Å of the radius reported by the supplier.

Optical Melting Curves

Melting curves were collected on a Hewlett-Packard 8450A diode array double-beam spectrophotometer interfaced to an IBM-AT personal computer. The sample and reference cuvettes were heated by thermostatically controlled cell holders. The heating rate was 18°C/h while absorbance at 268 nm was monitored. Identical temperature ramping of the sample and reference was performed by a Peltier temperature controller. Temperatures on melting curves are cell holder temperatures. Independent calibration with the temperature read from a thermocouple immersed directly in the sample fluid indicated the actual temperature of the sample never deviated more than 0.3°C from the sample holder temperature over the entire temperature range. Measurements (absorbance, temperature) were taken every 30 s (approximately every 0.15°C). The temperature range for each curve spanned from 10 to 75°C and each curve contained approximately 430 data points. For temperatures below

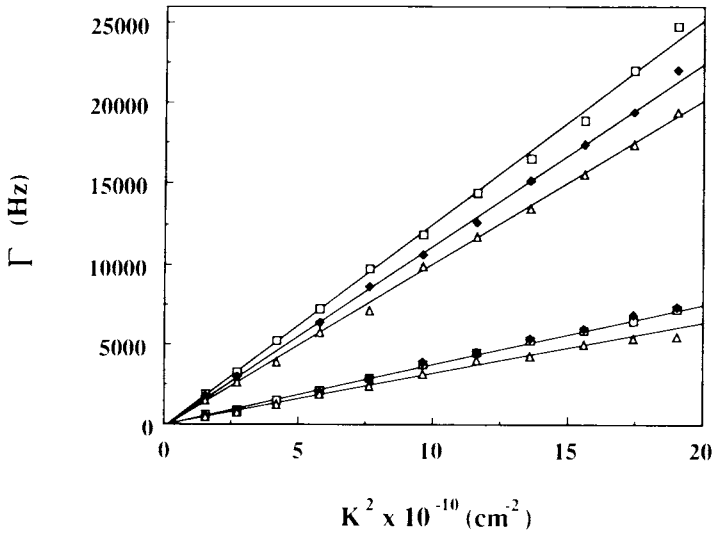

Figure 1. Relaxation rates of the fast (upper curves) and slow decaying components (lower curves) in M13mp19 ssDNA as a function of NaCl concentration. The NaCl concentrations are (□) 100 μM, (◆) 100 mM, and (△) 1.0M. All lines drawn through the data were determined from linear least-squares fits to all of the data as a function of K^2 and pass through the origin.

room temperature (21°C) the sample and reference cuvette holders were purged with N_2 gas to prevent condensation. Each melting experiment was done twice. Independent measurements of the entire spectrum from 220 to 400 nm were also made at a heating rate of ~ 20°C/h.

CD MEASUREMENTS

CD spectra were recorded in a Jasco (model J40a) spectropolarimeter. Wavelengths were scanned from 350 to 220 nm at a speed of 5 nm/min. All spectra were recorded at 20°C.

RESULTS

Biexponential Behavior and Reproducibility

As described in the appendix, the collected correlation functions at all scattering angles displayed biexponential behavior. Relaxation rates Γ_1 and Γ_2 and relative amplitudes a_1 and a_2 resulting from a biexponential analysis of the normalized field correlation function, $g^{(1)}(K, t)$, form the central foundation of our results. Diffusion coefficients D_i ($i = 1, 2$) were calculated from the Γ_i via

$$D_i = \Gamma_i / K^2 \qquad (1)$$

where K is the scattering vector. All reported D_i, unless specifically stated otherwise, were corrected using tabulated values[49] for the viscosity of NaCl to correspond to the viscosity of water at 20°C.

Although the results reported below were obtained on a single preparation of circular single strand M13mp19 DNA, a large portion of the reported results were produced, within experimental error, with a second DNA sample isolated from an independent phage growth performed six months after the first sample was prepared.

Effects of NaCl on Circular Single-Strand DNA

Relaxation Rates

The effect of changing the solvent ionic strength from 100 μM NaCl to 1.0M NaCl on the evaluated relaxation rates Γ_1 and Γ_2, is shown in Fig. 1, where Γ_1 and Γ_2 are plotted vs K^2 from 1.56×10^{10} cm^{-2} to 19.6×10^{10} cm^{-2}. Lines drawn through the data in Fig. 1 were determined from linear least-squares fits to all of the points. The plots clearly indicate that Γ_1 (the slow component) and Γ_2 (the fast component) are both linear functions of K^2 over the entire angular range and pass through the origin at $K^2 = 0$ in all salt environments examined. Similar linear plots of the relaxation rate vs K^2 were reported for linear double-stranded pUC8 DNA.[50] Such observations imply that contributions to the overall relaxation from rotational dif-

fusive motions of anisotropic ssDNA molecules are negligible. Γ_1 is taken to arise from global translational diffusive motions of the ssDNA that dominate the relaxation of the long wavelength fluctuations. Γ_2 is the relaxation rate of the (rather broadly defined) internal molecular subunits of the ssDNA that relax local, smaller wavelength fluctuations. Figure 1 shows that the relaxation rates of the slow component Γ_1, are apparently independent of NaCl concentration from 100 μM to 500 mM NaCl. A slight decrease in the slope of Γ_1 vs K^2 is observed in 1.0M NaCl, primarily due to the increased solvent viscosity in this salt environment. In contrast to Γ_1, the rates of the fast component Γ_2 vs K^2 decrease with each increasing NaCl concentration.

Relative Amplitudes

In Fig. 2 the relative amplitudes of the fast (lower curves) component and slow (upper curves) component in 100 μM, 100 mM, and 1.0M NaCl are plotted as a function of K^2. In the lower NaCl concentrations (and in 500 mM NaCl, data not shown), the respective relative amplitudes of the two components are virtually identical at all values of K^2. Figure 2 reveals that the difference between the fast- and slow-component amplitudes steadily decreases with increasing K^2, indicating the fast component contributes relatively more to the total relaxation as K^2 increases. The relative contribution of the slow-component amplitude is greater than that of the fast-component amplitude over the entire K^2 range, an observation that does not persist when the NaCl concentration is increased to 1.0M (see Fig. 2). Two interesting features of these curves emerge: (1) The slow-component amplitudes are less, over the whole K^2 range in 1.0M, than the amplitudes of the slow component in the lower salt environments ($\leq$ 500 mM NaCl), while the amplitudes of the fast component in 1.0M NaCl are larger than the relative amplitudes of the fast components in the lower NaCl environments. (2) Unlike what was observed in solutions of $\leq$ 500 mM NaCl, the relative amplitudes of the slow component as a function of K^2 are not greater than those of the fast component over the entire K^2 range. In fact, the curves for 1.0M NaCl in Fig. 2 cross at $K^2 \sim 16 \times 10^{10}$ cm^{-2} and at larger K^2 the relative amplitudes of the fast components exceed the slow-component amplitudes. Because the relative amplitudes of the relaxing components in ssDNA, as shown in Fig. 2, are related to the static scattering factors of ssDNA, the observed salt-induced changes in the relative amplitudes suggests that a rearrangement of the scattering elements takes place. Such changes are consistent with formation of substantial amounts of stable secondary structure on circular single-strand DNAs, especially in 1.0M NaCl. The result is a relatively larger contribution from the fast component to the overall relaxation in 1.0M NaCl than in lower salt environments ($\leq$ 500 mM NaCl). These relative amplitude values are employed later in converting experimental DLS data to a suitable

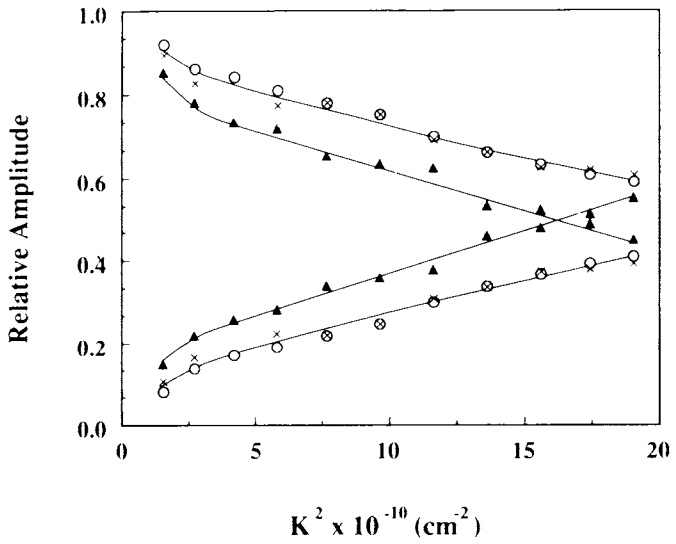

Figure 2. Relative amplitudes of the fast (lower curves) and slow (upper curves) decaying components in M13mp19 ssDNA in 100 μM (×), 100 mM (○), and 1.0M (△) NaCl.

Table I Experimental Parameters

[NaCl] (mM)	D_0[a] ($\times 10^8$ cm^2/s)	D_{plat}[a] ($\times 10^8$ cm^2/s)	R_G[b] (Å)
0.1	3.67	12.43	739
100	3.75	11.18	699
500	3.48	10.69	809
1000	3.39	10.26	830

[a] Values given are ±3%.
[b] R_G values are ±10 Å.

form for estimating (from the published algorithm[36]) parameters of the Rouse–Zimm model of Gaussian coils.

Diffusion Coefficients

Diffusion coefficients of the fast and slow modes, calculated from Γ_1 and Γ_2 and K^2, via Eq. (1), are listed in Table I and plotted vs K^2 in Fig. 3. As expected, the linear dependence of the relaxation rates on K^2 renders the diffusion coefficients of both the fast and slow components independent of K^2 in all salt environments.

The slow component diffusion coefficient is designated as D_0, the center of mass translational diffusion coefficient. As shown in Fig. 3, D_0 clusters around a value of $3.57 \times 10^{-8} \pm 0.14 \times 10^{-8}$ cm^2/s. Table I indicates the average value of D_0 in 1.0M NaCl at all angles defines the lower limit of this range (3.39×10^{-8} cm^2/s). The average D_0 in 100 mM NaCl (3.75×10^{-8} cm^2/s) lies near the top of the range stated above. D_0 values in 100 μM and 500 mM NaCl are between these limits. The 3% error involved in measuring D_0, as given in Table I, indicates D_0 is indistinguishable in 100 μM to 100 mM NaCl. D_0 is likewise indistinguishable in 500 mM and 1.0M, although the value is lower than that found in the lower salt environments.

In contrast to D_0, which changes slightly over the 10,000-fold range of NaCl concentration examined, the fast component diffusion coefficient shows a stronger dependence on the solvent ionic strength. In analogy with earlier DLS studies of double-stranded DNA,[33,36,37,51,52] these diffusion coefficients are designated as D_{plat} (for plateau). In terms of the Rouse–Zimm model, D_{plat} corresponds to the motions of the internal segmental subunits of the ssDNA.[36] As shown in Fig. 3, D_{plat} displays titratable decreases with increasing NaCl concentrations. In 100 μM NaCl the average over all K^2 of $D_{plat} = 12.43 \times 10^{-8}$ cm^2/s. D_{plat} decreases by 11% to 11.18×10^{-8} cm^2/s upon increasing the NaCl concentration to 100 mM. In 500 mM NaCl, D_{plat} decreases to 10.69×10^{-8} cm^2/s. Increasing the NaCl concentration to 1.0M induces D_{plat} to further decrease to 10.26×10^{-8} cm^2/s for an overall reduction of 22% from D_{plat} in 100 μM. The magnitude of the observed changes in D_{plat} are well outside the limits of experimental error of the measurements, which is in all cases ≤ 3%. Both D_0

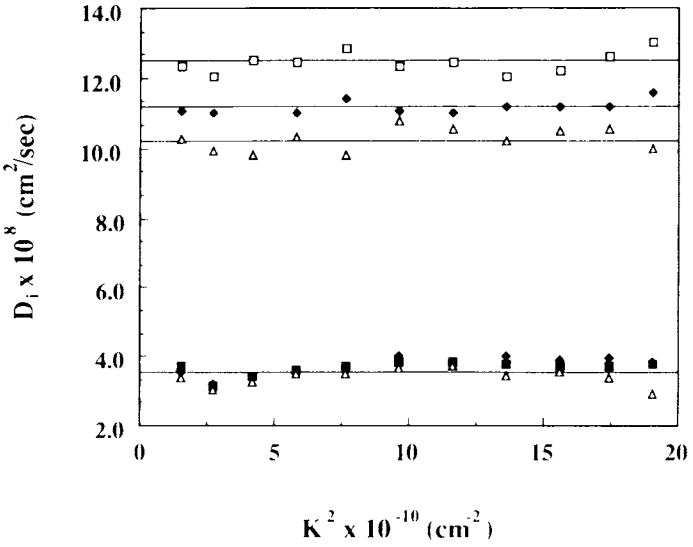

Figure 3. Diffusion coefficients of the fast (upper curves, $i = 2$) and slow (lower curves, $i = 1$) components in M13mp19 ssDNA. Horizontal lines drawn through the data indicate the average (over all K^2) value of the diffusion coefficients in the different NaCl environments. The symbols are (□) 100 μM, (◆) 100 mM, and (△) 1.0M NaCl.

and D_{plat} are employed below to estimate parameters of the Rouse–Zimm circular chain.

Radii of Gyration

Results of static light scattering measurements of single-strand M13mp19 viral DNA in salt environments from 100 μM to 1.0M NaCl are shown in Fig. 4. R_G values of the ssDNA molecules, determined from the slopes and y intercepts of the linear equations fit to the data in Fig. 4, are given in Table I. Experimental uncertainty of the reported R_G values (see Table I) was only ± 10 Å. In 100 μM NaCl, R_G = 739 Å. A 5% decrease in R_G was observed (R_G = 699 Å) when the NaCl concentration was raised to 100 mM, indicating that a slight contraction of the ssDNA global dimensions takes place when the NaCl concentration is increased from 100 μM to 100 mM.. This observation is analogous to the increase of D_0 in 100 mM from that in 100 μM. In 500 mM NaCl, R_G is 809 Å, 13% larger than it was in 100 mM and 9% greater than R_G in the 100 μM NaCl. In 1.0M NaCl R_G = 830 Å, a 3% increase over R_G in 500 mM NaCl environment.

Increases of this magnitude indicate effects of NaCl (over the range examined) on the global tertiary structure of ssDNA are subtle. The static light scattering measurements also confirm intermolecular aggregation (which would more strongly affect the y intercept in Fig. 4) and long-range intramolecular transitions (which would be expected to effect rather major changes in R_G) apparently do not occur at a detectable level. R_G values are also employed below to estimate Rouse–Zimm model parameters.

Melting Curves

Melting curves of circular single-strand M13mp19 DNA in NaCl environments from 100 μM to 1.0M are shown in Fig. 5. The relative absorbance changes of the DNA solutions from their initial absorbance at 268 nm at 10°C are plotted as function of temperature from 10 to 75°C. In Fig. 5 the magnitude of the relative hyperchromicity of each DNA sample is greater the higher the NaCl concentration of the solution. In 100 μM NaCl a 10% increase in hyperchromicity is observed. Raising the salt concentration to 100 mM results in an increase of 22%. A similar increase of 24% is observed in 500 mM NaCl. In 1.0M NaCl a most dramatic absorbance increase (> 40%) is observed.

Perhaps as revealing as the absolute differences in the relative absorbance increases observed in the four NaCl environments are the nontitratable differences in the shapes of the melting curves. In 100 μM NaCl the melting curve is nearly a linear function of temperature. In 100 and 500 mM NaCl the curves have a similar shape but deviate from linearity, with the deviation more pronounced on the 500 mM NaCl curve. In 1.0M NaCl a much

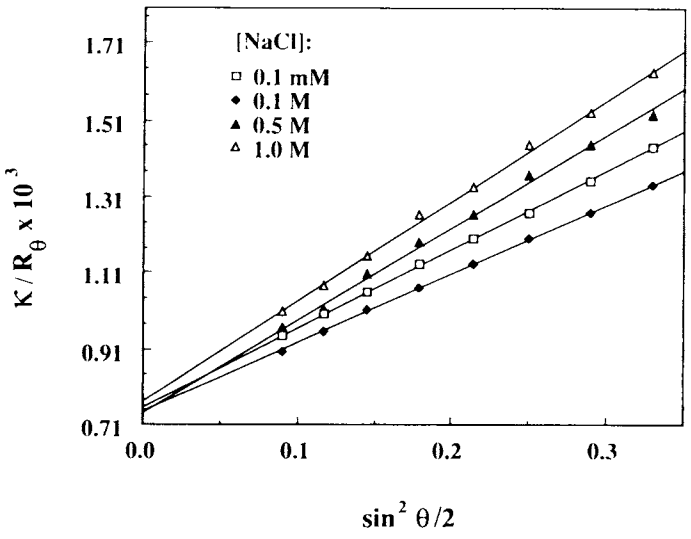

Figure 4. Results of static light scattering experiments. The ratio of the optical constant κ to the Rayleigh ratio R_θ, is plotted as a function of $\sin^2(\theta/2)$. The NaCl environments where the data were collected are indicated in the upper left corner. The slopes and y intercepts of these curves were used to calculate the R_G values given in Table I.

more sigmoidal melting curve, similar to what might be observed for a short linear double-stranded DNA,[53] is observed. These observations reveal an obvious increase of the cooperativity of the melting process of the ssDNAs with increasing NaCl concentration. Relative increases in melting cooperativity are likely to arise from the disruption of contiguously stacked regions of bases.

It should be noted in Fig. 5, for the melting curve in 1.0*M* NaCl, the total absorbance increase upon melting (> 40%) slightly exceeds the maximum possible absorbance at 268 nm (38%) determined as follows: The maximum absorbance change that can be expected for melting the circular ssDNA polymer was determined by digesting the polymer to mononucleotides with P1 nuclease. After correcting for the contribution to the absorbance from the enzyme, the total relative absorbance increase at 268 nm was determined to be only 38% (data not shown). The apparent discrepancy is not physically feasible if the absorbance at 268 nm is purely due to a hyperchromic effect. This apparent paradox was resolved by monitoring the entire spectrum of the ssDNA in 1.0*M* NaCl from 220 to 400 nm as a function of temperature. These measurements revealed a steady increase in the absorbance values from 300 to 400 nm with increasing temperature (data not shown), indicating a contribution from light scattering to the total absorbance at 268 nm. After correcting for the light scattering contribution in the standard way,[54] the relative hyperchromic increase in 1.0*M* NaCl (shown in Fig. 5) decreases by ~ 23% to 31% (data not shown). Similar observations were made for M13mp19 in 100 and 500 m*M* NaCl, although the light scattering contribution was considerably less. This increased scattering as a function of temperature is likely due to intermolecular aggregation of the ssDNA molecules. In support of this proposition, aggregation of double-stranded DNA in the melting transition region has been reported.[51,55,56] For the curves presented in Fig. 5, the absorbance correction at 268 nm has not been made. Involving the correction only serves to reduce the total relative absorbance increases but does not alter the curve shapes, the displayed trends, or alter the interpretations drawn from the melting curves. We are currently investigating this temperature-induced aggregation phenomena. Results of these ongoing investigations will be presented in a separate publication.

CD Spectra

CD spectra measured on M13mp19 ssDNA in 100 μM, 100 m*M*, 500 m*M*, and 1.0*M* NaCl are shown in Fig. 6. Three distinguishable features of these spectra can be readily identified. In all NaCl concentrations, the spectra display a major positive

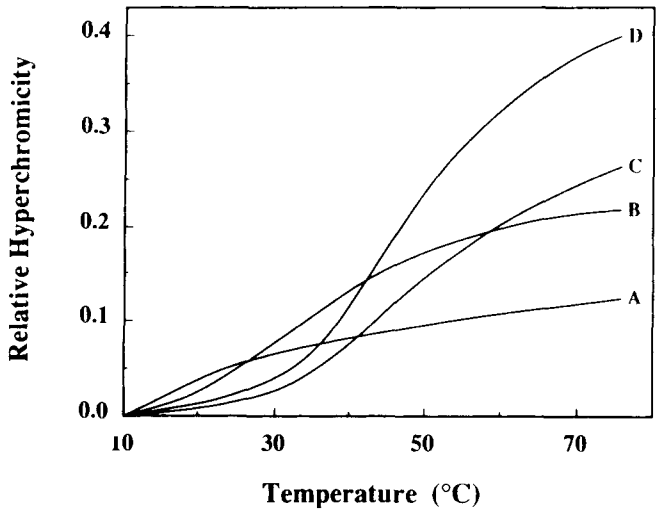

Figure 5. Melting curves of M13mp19 DNA as a function of NaCl concentration. Relative increase in absorbance (not corrected for light scattering) on the *y* ordinate is the fractional absorbance increase of the solutions as a function of temperature from the initial absorbance at 268 nm at 10°C. (A) The melting curve in 100 μM NaCl, (B) the 100 m*M* curve, (C) the 500 m*M* curve, and (D) the 1.0*M* curve. Note: curves (C) and (D) have not yet leveled off at 75°C, evidenced for the temperature-dependent aggregation phenomena described in the text.

band at 274 nm, a major negative band at 248 nm, and crossover from positive to negative rotational strength between 258 and 261 nm. The crossover point is salt dependent. On all spectra the rotational strength of the positive band is approximately 25% greater than that of the negative band. Such a disproportion between the positive and negative rotational strengths of the CD spectrum has been reported for denatured double-stranded DNA,[57] and generally resembles CD spectra displayed by double-stranded RNA or DNA in an A-like conformation.[58,59]

Of the CD spectra in Fig. 6, the most distinct difference is observed for the positive band. On the 100 μM and 100 mM spectra the rotational strength is approximately 9% less than the positive band intensities obtained in the higher NaCl environments. In 500 mM up to 1.0M NaCl the strength of the positive band is approximately the same. The increased rotational strength observed in going from 100 μM and 100 mM NaCl to 500 mM necessarily indicates an increase in the amount of base stacking.[57] The crossover wavelength from positive to negative rotational strength (the intercept of the CD spectrum at zero ellipticity) is slightly shifted to the blue from 261 nm in 100 μM to 258 in 1.0M. This blue shift of the crossover wavelength indicates an increased stability of base stacking as the NaCl concentration is increased.[57]

Evaluation of Rouse–Zimm Model Parameters

The Rouse–Zimm model consists of a collection of beads or Gaussian subunits connected by massless springs. The model is founded on three fundamental parameters. These are $N + 1$, b, and f. $N + 1$ is the number of Gaussian subchains, b the rms subchain displacement (or mean separation of the beads), and f the friction factor of the individual subchains.[36]

Application of the Rouse–Zimm model to the analysis of DLS of double-stranded DNA was developed and first reported by Lin and Schurr.[36] Since its introduction this model has been applied by these[37,51,59] and other investigators[61,62] to analyze the behavior of linear double-stranded DNA in various solvent environments. These studies lend credibility to the proposition of applying the model to analyze DLS of ssDNA, although, as given subsequently, several assumptions must be made in the latter case.

An assessment of the actual conformity of the experimental results with ideal Rouse–Zimm coil behavior can be made (at small K^2) by considering for a sufficiently long Rouse–Zimm chain the center of mass translational diffusion coefficient D_0^{RZ} is inversely related to R_G by[35]

$$D_0^{RZ} = k_B T/6\pi\eta(.677)R_G \qquad (2)$$

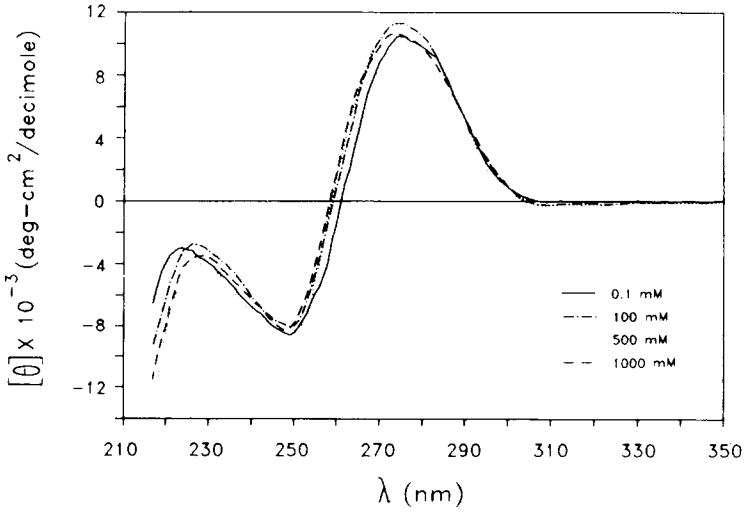

Figure 6. CD spectra of M13mp19 DNA at 20°C as a function of NaCl concentration. The mean residue ellipticity with units of deg · cm^2/decimole nucleotide is plotted on the y axis vs the wavelength, λ, from 220 to 330 nm. Relevant features of the spectra are described in the text.

Table II Rouse–Zimm Model Parameters[a]

[NaCl] (mM)	b[b] (Å)	f[b] [$\times 10^7$ (dyne · s/cm)]	$D_0^{R_z}/D_0$[c]	$D_{seg} = k_B T/f$[d] ($\times 10^8$ cm^2/s)	P[e] (Å)
0.1	467	2.59	1.17	15.65	191
100	442	2.78	1.21	14.58	181
500	512	3.01	1.13	13.43	210
1000	524	3.13	1.13	12.94	215

[a] The number of Gaussian subchains was fixed at $N + 1 = 15$ in evaluating the parameters shown.

[b] The accuracy of b and f as estimated (see text) may be no better than $\pm 30\%$. The relative values are significant.

[c] Represents the ratio of the center of mass translational diffusion coefficient for an ideal Rouse–Zimm chain, $D_0^{R_z}$, calculated from the measured R_G (see text), to the measured center-of-mass translational diffusion coefficient D_0.

[d] D_{seg} calculated from f is the free-subunit diffusion coefficient.

[e] P, the persistence length, was calculated from b as described in the text.

With the experimentally measured values of R_G given in Table I, D_0^{RZ} at each salt concentration can be readily obtained. The ratios of D_0^{RZ} to the directly measured D_0, D_0^{RZ}/D_0, determined at each NaCl concentration, are given in Table II. Values of D_0^{RZ}/D_0 indicate that a 13–21% higher center of mass diffusion coefficient is predicted from R_G by the model than is actually observed. Verification of the model behavior in the large K^2 region is less direct.

Since the high K^2 region of the curve could not be experimentally probed, the scheme to follow relies on two basic assumptions: (1) the behavior of a circular ssDNA can be reasonably simulated (within the deviation given above) by a circular Rouse–Zimm model chain, and (2) the small departure of circular ssDNA from ideal Rouse–Zimm behavior does not vary wildly over and beyond the experimentally accessible region of the scattering curve up to $D_{app} = D_{plat}$. If the analysis is not invalidated under this umbrella of assumptions, a semiquantitative estimate of the Rouse–Zimm model parameters for circular ssDNA, utilizing our experimental parameters, namely D_0 and D_{plat} along with R_G (see Table I), can be made.

A straightforward algorithm for evaluating $N + 1$, b, and f was presented by Lin and Schurr.[36] Use of their algorithm requires experimental measurements of the apparent diffusion coefficient $D_{app}(K^2)$ vs K^2. D_0 (D_{app} ($K^2 = 0$)) and D_{plat} (the asymptotic value of D_{app} at large K^2) are directly determined from these curves. The analysis is founded on determination of $D_{app}(K^2)$ from the relaxation rates evaluated by single exponential fitting of the experimental correlation functions as a function of K^2. Because D_{plat} is the asymptotic value of D_{app} at large K^2, an accurate evaluation of D_{plat} requires that D_{app} actually reach a clearly resolved plateau within the experimentally accessible region of K^2 ($K^2 \leq 20 \times 10^{10}$ cm^{-2}). Such is the case for the long double-stranded DNAs studied by Schurr and co-workers.[36,37,51,60] In the present study of circular ssDNA, as demonstrated subsequently, the experimental data do not entirely support an analysis of the type employed by Schurr and co-workers.[36,37,51,60]

The curve shown in Fig. 7 of D_{app} vs of K^2 in 1.0M NaCl was constructed from the corresponding experimentally evaluated D_0, D_{plat}, and relative amplitudes a_1 and a_2 as follows: At each value of K^2, D_{app} was evaluated numerically by setting the double exponential function of the relaxation rates Γ_1 and Γ_2 in time to a single exponential with a single relaxation rate Γ_{app}, viz.

$$a_1 \exp(-\Gamma_1 t) + a_2 \exp(-\Gamma_2 t) = A \exp(-\Gamma_{app} t) \tag{3}$$

where a_1 and a_2 are the relative amplitudes of the slow and fast components (Fig. 2), and A is the amplitude coefficient of the single exponential. Since a_1 and a_2 are relative amplitudes, $a_1 + a_2 = 1$, and the condition at $t = 0$ therefore requires that $A = 1$. The relaxation rates in Eq. (3) have the following definitions:

$$\Gamma_1 \equiv D_0 K^2 \tag{4a}$$

$$\Gamma_2 \equiv D_{plat} K^2 \tag{4b}$$

$$\Gamma_{app} \equiv D_{app} K^2 \tag{4c}$$

To evaluate Γ_{app}, Eq. (3) was calculated in 100 ns

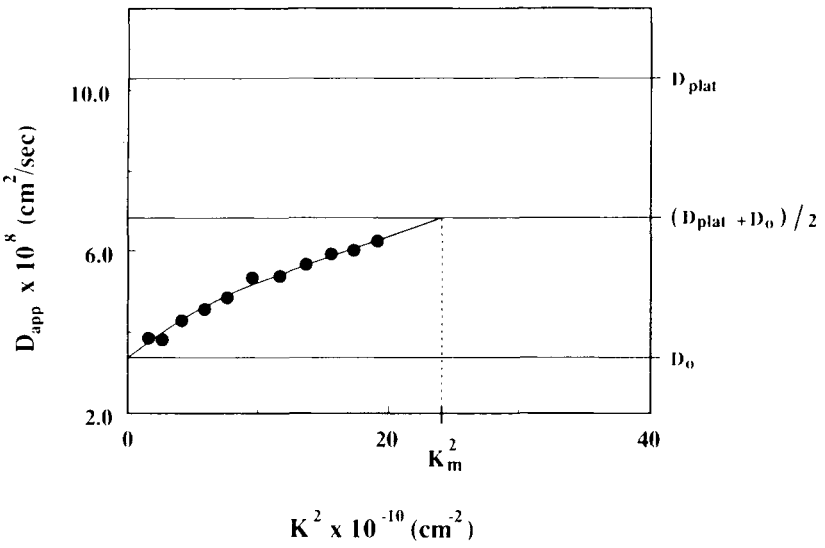

Figure 7. Plot of D_{app} vs K^2 for M13mp19 circular ssDNA in 1.0M NaCl constructed from the exponential data as described in the text. Points fit by the solid line were obtained from the experimental data. The dashed line extending beyond the data was extrapolated from the slope of the line fit to the last five data points. Where this extrapolated line of D_{app} vs K^2 intersects $D_{app} = (D_{plat} + D_0)/2$ determines the value of K_m^2. $K_m^2 = 24.1 \times 10^{10}$ cm^{-2}.

steps for $t = 100$ ns to 2 ms. The value of $t = 1/\Gamma_{app}$ was obtained when the right-hand side of Eq. (3) equaled $1/e = 0.3678794$. From Γ_{app} vs K^2, D_{app} was determined from Eq. (4c) and plotted in Fig. 7. Not surprisingly, the curve in Fig. 7 and that derived from a single exponential analysis of the data were virtually identical over the comparable K^2 region.

Figure 7 is the D_{app} vs K^2 curve in 1.0M NaCl. Depicted for reference on this curve are the values of the average (over all angles) of D_0 and D_{plat} in 1.0M NaCl. The point of D_{app} halfway between D_0 and D_{plat} ($D_{app} = (D_0 + D_{plat})/2$) is also indicated. As shown in Fig. 7, D_{app} vs K^2 displays a considerable slope at $K^2 = 20 \times 10^{10}$ cm^{-2}. This renders it difficult to estimate with any great certainty where the D_{app} vs K^2 curve actually levels off and reaches a plateau. This limitation can be overcome if we assume that D_{plat}, evaluated from the relaxation rate of the fast component, is the true plateau diffusion coefficient.

In the algorithm provided by Lin and Schurr,[36] b^2, the mean squared displacement of the beads, is evaluated graphically from the plots of D_{app} vs K^2 from the value of $K^2 = K_m^2$, where $D_{app} = (D_0 + D_{plat})/2$ by

$$b^2 = 8/K_m^2 \qquad (5)$$

Because the plot of D_{app} vs K^2, calculated from the experimental data (as shown in Fig. 7) does not extend to K_m^2 ($D_{app} = 6.83 \times 10^{-8}$ cm^2/s), values of D_{app} were obtained from linear extrapolation over higher K^2 to this point. The slope used for the linear extrapolation was determined from a linear least squares fit made to the last five points on the curve ($K^2 \geq 10 \times 10^{10}$ cm^{-2}). The symbols in Fig. 7 are the points determined from the actual experimental data. Extrapolated portions of the curves in Fig. 7 are shown as dashed lines. The graphical evaluation of $K_m^2 = 24.1 \times 10^{10}$ cm^{-2} is also depicted in Fig. 7. It should be noted that performing this linear extrapolation of D_{app} vs K^2 to evaluate K_m^2 necessarily provides the lower bound of K_m^2. Since the curve of D_{app} vs K^2 should asymptotically (not linearly) approach D_{plat} at large K^2, the actual value of K_m^2 could actually be larger than that obtained from mere linear extrapolation. Therefore, it should be noted that K_m^2 is necessarily a lower bound and b evaluated from K_m is an upper bound on this Rouse–Zimm parameter. Indeed, this graphically evaluated value of b (576 Å) does slightly exceed the value of b given in Table II (524 Å) estimated from R_G with $N + 1 = 15$ as described below. Although the curves of D_{app} vs K^2 in the lower salt environments were qualitatively similar to the curve in 1.0M NaCl, an even larger extrapolation than that

in 1.0M NaCl was required in 500 mM, 100 mM, and 100 μM NaCl. For this reason the scheme provided by Lin and Schurr[36] for evaluating b directly from plots of D_{app} vs K^2 could not be reliably applied. However, assuming the number of Gaussian subchains, $N + 1$, does not change with NaCl concentration, b and f can be determined from the evaluated R_G, D_0, and D_{plat}. For a Rouse–Zimm chain, b is related to R_G and the number of Gaussian subunits, $N + 1$, by[36]

$$b = [(N + 1)/6]^{1/2} R_G \qquad (6)$$

$N + 1 = 15$ is assumed throughout and from the values of R_G given in Table I, the values of b given in Table II were derived.

As has been previously indicated,[36,51] b depends inversely on the static flexibility of the chain and is therefore sensitive to changes in the persistence length P. An increase in b indicates an increase in P. From the values of b given in Table II, a lower bound on the persistence length of the single-strand DNA in each NaCl concentration can be estimated.

For a section of worm-like coil of contour length $\mathscr{L}$, the rms end-to-end distance, $\langle L^2 \rangle$, is given by[51,63]

$$\langle L^2 \rangle = 2P[\mathscr{L} - P + P\exp(-\mathscr{L}/P)] \qquad (7)$$

It is required that the smallest conceivable Gaussian subchain must contain at least two statistical lengths, λ ($\lambda = 2P$[51]). Thus assigning $\mathscr{L} = 2\lambda = 4P$ in Eq. (6) yields $b = \langle L^2 \rangle^{1/2} = 2.44P$.[51] From the b values given in Table II, the persistence lengths given in Table II were evaluated from Eq. (7). Obviously, the absolute values of b (or P) are model dependent. Therefore, values of b and P given in Table II are likely to be only accurate (within ~ 30%) because of the approximations involved in their evaluation. The relative values of these parameters and the trend displayed are more meaningful.

The last parameter of the Rouse–Zimm model to be estimated, f, the hypothetical friction factor of the internal subunits if they could freely diffuse unconnected in solution, is evaluated from an expression provided by Lin and Schurr.[36] For a circular Rouse–Zimm chain the difference between D_{plat} and D_0 is given by[36]

$$D_{plat} - D_0 = (k_B T/f)(N/N + 1) - W(b, N + 1)) \qquad (8)$$

where k_B is the Boltzmann constant and $W(b, N + 1)$ is the correction of the hypothetical diffusion coefficient for the independent random local displacements of the Gaussian segments, $D_{seg} = k_B T/f$, required by the model for the presence of hydrodynamic interactions. When $N + 1$ is sufficiently large (≥ 10), Lin and Schurr[36] provided

$$W(b, N + 1) = F/b(N + 1)^{1/2} \qquad (9)$$

where F is a universal constant for the circular Rouse–Zimm chain ($F = 1.06 \times 10^{-12}$ cm^3/s). F is independent of b, $N + 1$, and f, but proportional to T/η. With the appropriate values of b and $N + 1$, W is evaluated from Eq. (9). From W, D_{plat}, and D_0, f can be determined from Eq. (8). Table II indicates the friction factors of the internal segments increase with increasing NaCl concentration which reduces the diffusive mobility of the chain segments resulting in a decreasing D_{seg}.

DISCUSSION

Secondary Structure in ssDNA

Combining the complementary results of the optical melting experiments in Fig. 5 with the CD spectra in Fig. 6, characteristics of the ssDNA local structure as a function of NaCl can be inferred. In the lowest ionic strength environment, 100 μM NaCl, electrostatic repulsion between phosphate residues of the DNA backbone is strong. Coulombic repulsion between these residues considerably extends the structure, thereby preventing establishment of stacking interactions between base residues along the DNA or base pairing between complementary sequence sections. The result is a polymer with limited flexibility along the DNA. Stacking interactions or hydrogen bonds that could form between the bases in this NaCl environment would be expected to be quite unstable.

When the ionic strength of the surrounding solvent is increased to 100 mM NaCl, sodium ions considerably reduce repulsion between the phosphates and exclude some of the water from the backbone surface. These events provide better conditions for base encounters and establishment of stacking interactions along the ssDNA strand. The CD spectra indicate base stacking does not increase in 100 mM NaCl over what was found in 100 μM. The melting curve in this salt essentially agrees and indicates the stacking that does form is fairly

unstable and short range. The reduction in the electrostatic repulsive force causes a slight contraction of the global dimensions resulting in an observed decrease of R_G in 100 mM NaCl. Above 100 mM the CD spectra indicate a significant increase in both the amount and stability of the stacking formed at 20°C.

As mentioned above, the relative hyperchromicity on melting curves in $\geq$ 100 mM NaCl (Fig. 5) verifies increases in stability of the stacking interactions. The observed cooperativity of the melting curves further provides a qualitative indication of the relative size of the cooperative units formed along the ssDNA. Cooperative units are taken to be regions along the ssDNA comprised of contiguously stacked nucleotides that melt as a single block. As the length, number, and collective stability of the cooperative units increases so does the relative cooperativity of the hyperchromicity resulting from their disruption as the temperature is elevated. Obviously, the melting curve in 1.0M NaCl indicates a substantial increase in the size of domains containing stacked residues over the lower NaCl environments. While the CD appears fairly insensitive to the proposed increase (nearly 20%) in base stacking, it does not contradict this proposition for the following reason.

Because CD is inherently a local effect due to nearest-neighbor and next nearest-neighbor nucleotide base interactions, short sections on the order of only three to five bases long give rise to the spectral signal.[64] Consequently, CD is fairly insensitive to the additional presence of more than three to five nucleotide residues stacked together. Therefore formation of domains containing relatively longer contiguous stretches of stacked residues, as was postulated to occur in 1.0M NaCl, do not greatly affect the observed CD spectra. CD is thus quite sensitive to the type and strength of stacking that takes place in DNA but not to the number of residues (above five or so) comprising the stacked regions. Melting curve analysis, on the other hand, provides complementary information concerning the total number of stacked residues, their contiguous arrangement, and their thermodynamic stability.

Results of DNA polymerase mapping experiments combined with computer-assisted nucleotide sequence analysis of M13mp8 viral DNA have been reported.[27] M13mp8 contains 7229 bases and is identical to M13mp19 used in the present studies except for the different polylinker regions of the two ssDNAs. On the basis of nucleotide sequence analysis alone, 10^5–10^6 regions having partially self-complementary or palindromic sequences capable of intramolecular hydrogen bonding were identified. In addition, DNA polymerase pausing experiments demonstrated that many of these computer-predicted regions of secondary structure actually correspond to sites capable of pausing the action of DNA polymerase α. Finding sites common to DNA polymerase pausing and computer-predicted secondary structure strongly implicates these regions in adopting intramolecular hairpin structures.

Increases in base stacking as the NaCl concentration is increased would necessarily track with the salt-induced formation and stability of hairpin secondary structures on single-strand M13mp19 DNA. In this regard, results of our CD and optical melting curve experiments are entirely consistent with the findings of the published studies mentioned above. What has not been previously reported are the effects of this increased stacking and suspected intramolecular hairpin formation on the global tertiary structure and internal dynamics of circular ssDNA.

Tertiary Structure

The changes in D_0 and R_G observed for circular ssDNA from 100 μM to 100 mM NaCl resemble the behavior of linear double-stranded DNA within this range of Na^+ concentration. For double-stranded DNA, as the salt concentration is reduced below 10 mM Na^+, the persistence length P, which is directly proportional to R_G and inversely related to D_0, increases,[65] just as we observed for circular ssDNA from 100 mM to 100 μM NaCl. Because of the dominant effects of phosphate repulsion on the circular ssDNA structure and the associated excluded volume effects, the molecule has access to a limited range of global conformations as it meanders through solution under the influence of Brownian motion. The increase in R_G and decrease in D_0 in 100 μM (NaCl) from the values in 100 mM is consistent with a more extended global structure with limited flexibility.

The behavior of circular ssDNA above 100 mM NaCl seems to differ from that of linear double-stranded DNA. Published studies of linear *Col E1* double-stranded DNA indicate a steady *decrease* of R_G (and P) over the range from 7 mM to 1.0M Na^+[66], the opposite trend we saw for ssDNA above 100 mM NaCl.

The directly opposite salt-dependent hydrodynamic behavior of double-stranded vs single-

strand DNA obviously underscores the structural differences between the two DNA forms and the forces stabilizing them. In essence, the electrostatic contribution to the persistence length from phosphate repulsion in double-stranded DNA acts to stiffen the DNA. In double-stranded DNA, increasing amounts of Na^+ screen the repulsion, affording more flexibility to the molecule, resulting in a reduced persistence length.[67] However, only in the lowest NaCl environment (100 μM) should the electrostatic persistence length make a non-negligible contribution to the total observed persistence length.[67] Increasing salt in ssDNA solutions (above 100 mM NaCl) and consequent screening of the electrostatic repulsion leads to increased base stacking, which stiffens the molecule, thereby increasing its observed persistence length. Increased stacking in homopolymer RNAs was also shown to result in an increase of R_G,[68] just as we observed.

The D_0 we determined is more than a factor of two less than D_0 of the very similar, but smaller, M13 wild-type and fd DNAs previously evaluated from hydrodynamic measurements.[20,21] These authors reported $D_0 \approx 8.25 \times 10^{-8}$ cm^2/s after correction to the viscosity of water at 20°C. M13mp19 contains 7250 nucleotides, 843 more than wild-type M13, which corresponds to only a 12% increase in the molecular weight. Since our M13mp19 ssDNA samples displayed no signs whatsoever of intermolecular aggregation or contamination with high molecular weight DNA, nor did the ssDNAs appear to be molecular dimers, this decrease in D_0 for M13mp19 from that previously reported for M13 wild-type must be interpreted as reflecting a substantial increase in the overall hydrodynamic dimensions, and therefore the global frictional drag, of M13mp19 over wild-type M13 and fd ssDNA.

The relaxation rates of the center of mass motion Γ_1, are linear functions of K^2 and pass through the origin. This behavior for circular ssDNA is analogous to that observed in DLS experiments of linear double-stranded pUC8 DNA,[50] and inferred to be an indication that the global structure and the associated long-range motions are largely isotropic. Therefore contributions to the relaxation at small K^2 from rotational diffusive processes are not detectable, at least in the polarized DLS experiments. Because our data and other published data implicate the formation of intramolecular hairpins, the observations stated above immediately suggest if intramolecular hairpins do form, the majority of such structures are likely to extend over a short range, formed between closely adjacent self-complementary single-strand regions. Establishment of a number of such relatively short regions (~ 30–300 bases) would not be expected to greatly influence the global tertiary structure, and would also be consistent with our melting and CD data. From our data we cannot definitely conclude if intramolecular hairpins form at all. However, our data do argue that if hairpins do form, these are not long-range structures that would necessarily be expected to induce substantial changes in D_0, R_G, and the behavior of Γ_1 as a function of K^2 *which* are not observed.

Internal Dynamics

While the tertiary structure of M13mp19 ssDNA is only slightly sensitive to the changes in local structure brought about by increases in NaCl concentration from 100 μM to 1.0M, motions of the internal subunits of ssDNA are more strongly affected. Because the fast relaxation rates Γ_2, are also linear functions of K^2, the plateau diffusion coefficient D_{plat}, calculated from them is essentially constant at all values of K^2. The slopes of the Γ_2 vs K^2 curves, however, decrease with each increase in NaCl concentration, causing D_{plat} to decrease proportionally. After viscosity corrections, D_{plat} still displays significant decreases with increasing NaCl concentration. As previously mentioned and illustrated subsequently, D_{plat} represents motions of internal segments or subunits of the ssDNA.[36] The titratable decreases with increased NaCl observed for D_{plat} reveal an impedance of the subunit motions. Consistent with our data, the formation of stacking interactions must act to substantially restrict many of the internal motions within segments and thereby reduce the number of modes available to relax small wavelength fluctuations. Consequently, the time $\tau = 1/\Gamma_2$ required for the motions of the subunits to relax fluctuations that occur over a distance $1/K$ (when $R_G^2 K^2 \gg 1$) increases, resulting in a diminished value of D_{plat}.

The relative amplitudes of the fast relaxing component a_2, indicate the relative contribution of motions monitored by Γ_2 to the total relaxation. At NaCl concentrations below 500 mM, factors responsible for impeding internal motions and their relaxation rates do not have an effect on the scattering properties that contribute to a_2, and a_2 remains unchanged as a function of NaCl concentration. The sharp increase in a_2 (from 40 to 60% over the entire range of K^2) that is observed when the NaCl concentration is increased to 1.0M indicates a substantial increase in the scattering ampli-

tude of the internal segments. Such an increase suggests a significant rearrangement of the scattering elements probably due to formation of domains of stacked bases along the strand and or intramolecular hairpins. These structures apparently not only impede internal motions of the subunits, they act to increase the scattering amplitude of the segmental motions of ssDNA. Interpretations of the experimental data given so far are imminently plausible on intuitive grounds and also supported (for the most part) by parameters of the circular Rouse–Zimm chain evaluated from the experimental data as given in Table II.

In 100 μM NaCl the circular Rouse–Zimm chain comprised of 15 Gaussian subunits has a rms extension, b, between that in 100 and 500 mM NaCl, a finding consistent with the measured values of R_G and D_0. The hypothetical segmental diffusion coefficient, k_BT/f, is the largest in 100 μM NaCl, indicating the relatively greatest diffusive mobility of the chain elements. Apparently, in 100 μM NaCl the electrostatic repulsive force not only extends and stiffens the ssDNA molecule, it also prohibits formation of stacking interactions. The result is a globally less flexible structure with considerable freedom of motion per subunit.

Screening of the electrostatic repulsion in 100 mM NaCl acts to increase the static flexibility of the Rouse–Zimm chain. The decreased b reveals, although base stacking is not strong enough in 100 mM NaCl to greatly effect the overall flexibility, transient local structures impede the small wavelength motions available to relax small wavelength fluctuations, which causes a decrease in k_BT/f.

Raising the NaCl concentration to 500 mM changes the situation from that in 100 mM. With the number of subunits held constant at $N + 1 = 15$, the static flexibility of the circular Rouse–Zimm chain decreases considerably, as indicated by the increased value of b. Meanwhile, the motions of the internal subunits also decrease due to increased stacking. This observation, along with an increase in R_G, probably indicates not only an increase in the stability of the stacked bases that formed in 100 mM NaCl but also the formation of significantly more stacked bases.

In 1.0M NaCl (as the melting curve in Fig. 5 indicates), substantially more base-stacking forms than in the lower ionic strengths. Elongated regions that contain contiguous sections of stacked bases are formed along the ssDNA that act to greatly reduce the static flexibility of the circular chain indicated by the increased value of b. The less flexible chain has an increased R_G. This additional stacking also acts to impede motions of the internal subunits that decreases k_BT/f.

CONCLUSION

Results of this study indicate that the observable changes in M13mp19 ssDNA structure and dynamics that occur from 100 μM NaCl to 1.0M NaCl are primarily associated with local structural rearrangements that do not greatly perturb the overall global tertiary conformation of circular ssDNA. This behavior could be biologically relevant. For example, significant local structural changes not coupled to global tertiary conformation could provide avenues for interactions with regulatory proteins and ligands within the cell where the ssDNA tertiary structure may be considerably constrained. Now that a detailed characterization of the structure, dynamics, and Rouse–Zimm model behavior of M13mp19 circular single-strand DNA has been performed, it will be interesting to apply this information in investigating perturbations induced in the single strand by interactions with regulatory proteins such as single strand binding protein and RecA protein. Such investigations are currently underway.

APPENDIX

Collection and Analysis of Dynamic Light Scattering Data

All of the data analysis subsequently described was entirely performed on an IBM-AT personal computer using the software routines developed and generously provided by Professor Paul Russo (Chemistry Department, Louisiana State University).

Photon correlation functions were collected over 272 delay channels at two different sample times. Photon-pulse count rates typically varied from 20,000 to 80,000 counts per second. The first 256 channels collected the decaying correlation function in real time while the last 16 channels were delayed 256 sample times and collected the baseline. Sample times were adjusted according to the value of the z-average relaxation rate or first cummulant,[69] and set such that 256 channels spanned at least six relaxation times of the collected correlation function. Although a detailed investigation of the effects on our results of using different experimental sample times was not performed, sample times routinely varied over a factor of two provided essentially indistinguishable results. Sets

of 8–12 correlation functions were collected at 10° increments over the entire accessible range of scattering angles θ ($30° \leq \theta \leq 140°$). Collection time for the individual runs at each angle was constant and ranged from 2 to 6 min, depending on the count rate at that particular angle. Collection of the complete light scattering curve took about 8 h.

Our count rate meter served as the primary means of dust discrimination. It can be set to a threshold count rate and halt collection of the autocorrelation function when the threshold is exceeded. In all of our experiments the threshold was set to 20% above the mean count rate.

To gain a quantitative sense of the overall quality of the data, a second cummulants analysis of each individual correlation function in a set was performed.[69] To minimize effects of ion-induced after pulsing in the photomultiplier,[51] the first channel was always excluded and the fits were made to the remaining 255 channels, yielding the second cummulant and the corresponding relaxation rate. Statistically weighted chi-squared (χ^2)[70] of the fits were consistently between 0.7 and 1.3, while percent variance of the relaxation rate from one run to the next within a set was less than 2%.

The experimental baseline B_e was determined as the average of the number of counts in each of the 16 delay channels. When compared with the theoretically calculated baseline B_t (obtained from the total squared intensity) the relative difference between B_t and B_e, $|B_t - B_e|/B_t$ was always ≤ 0.003. Individual correlation functions within each set were summed and subjected to exponential fitting as subsequently described. The sums of the individual B_t's within each set were also determined for use in subsequent analysis.

Exponential Fitting of the Data

In the homodyne light scattering experiment, the measured (unnormalized) second-order photon autocorrelation function, $G^{(2)}(K, t)$ is given by[52]

$$G^{(2)}(K, t) = \langle n(K, t)n(K, t + n'\Delta\tau)\rangle$$

$$= \langle n\rangle^2\left(1 + F(A)\left|g^{(1)}(K, t)\right|^2\right) \quad \text{(A1)}$$

$\langle n(K, t)n(K, t + n'\Delta\tau)\rangle$ is the time average product of the number of photon pulses that occur (at a particular scattering angle) in two equal nonoverlapping sampling intervals, short with respect to the relaxation time and separated by a delay time, $n'\Delta\tau$. $n' = 1{,}256$ and $\Delta\tau$ is the correlator channel sample time. $\langle n\rangle^2$ is the correlation function baseline. In our case $G^{(2)}(K, t)$ is the summed correlation function. $F(A)$ is an experimental constant that depends on the number of coherence areas in the detected scattering volume.[71,72] For the scattering volume defined by our focused beam and detection optics, $F(A) \sim 1$.

The first-order normalized field correlation function $g^{(1)}(K, t)$ in Eq. (A1) is given by a sum of exponential decays, that is

$$g^{(1)}(K, t) = \sum_{i=1}^{N} a_i \exp(\Gamma_i t) \quad \text{(A2)}$$

where a_i is the amplitude of the ith decay process with a decay rate Γ_i. Routinely in our analysis we fit both $G^{(2)}(K, t)$ and $g^{(1)}(K, t)$ with exponential functions. The Marquardt nonlinear least-squares algorithm as described by Bevington[70] was employed.

$G^{(2)}(K, t)$ Fits

Neglecting the first channel, each 255 point $G^{(2)}(K, t)$ was fit with a sum of exponentials and a floating baseline B_f, of the form

$$G^{(2)}(K, t) = B_f + \sum_{i=1}^{N} A_i \exp(2\Gamma_i t) \quad \text{(A3)}$$

For $N = 1$, 2, and 3, fits of $G^{(2)}(K, t)$ were performed using B_f and the corresponding A_i's and Γ_i's as adjustable parameters.

The value of B_f evaluated from the exponential fits of $G^{(2)}(K, t)$ appeared to be virtually independent of the order of exponential function used in the fit and accurately agreed with the theoretical baseline B_t, evaluated from the square of the average intensity. The relative difference $|B_f - B_t|/B_t$ for either single, double, or triple exponential fits was ≤ 0.001 ($> 95\%$ of the cases). Such an observation indicates the resolvable relaxing components comprising the correlation function have all sufficiently decayed in the collection time to allow an accurate baseline determination. Typical values of B_t ranged from $1–5 \times 10^5$ counts. Values of the statistically weighted χ^2 of the $G^{(2)}(K, t)$ fits indicated the smallest value and therefore the best fit at all scattering angles was obtained with a biexponential. Single exponential fits produced χ^2 75% larger than the double exponentials while three exponential fits did not significantly reduce χ^2 from that obtained with the biexponential analysis.

Even though the baseline, B_f, appeared to be accurately evaluated from the biexponential fits of

$G^{(2)}(K, t)$, the signal to noise ratio in $G^{(2)}$ is apparently insufficient to allow consistently reliable evaluation of the relaxation rates Γ_1 and Γ_2. Independent biexponential analysis of specifically prepared bimodal mixtures of polystyrene spheres (data not shown) also demonstrated that relaxation rates and relative amplitudes are more accurately evaluated from biexponential fits of $g^{(1)}(K, t)$ than $G^{(2)}(K, t)$. We therefore employed exponential analysis of $g^{(1)}(K, t)$ instead of $G^{(2)}(K, t)$ to extract the desired relaxation rates and relative amplitudes. In our analysis, however, $G^{(2)}$ fitting was always done prior to $g^{(1)}$ fitting to evaluate the baseline.

$g^{(1)}(K, t)$ Fits

Using the baseline B_f, determined from the fits of $G^{(2)}(K, t)$, the value of $g^{(1)}(K, t)$ was calculated from Eq. (A1) with $\langle n \rangle^2 = B_f$,

$$g^{(1)}(K, t) = \left(\left(G^{(2)}(K, t) - B_f\right)/B_f\right)^{0.5} \quad \text{(A4)}$$

As for the $G^{(2)}$ fits, exponentials of the form given in Eq. (2) with $N = 1, 2$, and 3 were fit to the $g^{(1)}$'s in Eq. (4) using the Marquardt algorithm.[70] The curves of $g^{(1)}$ resulting from each exponential fit were examined to determine which produced the minimum in the statistically weighted χ^2. As was the case for $G^{(2)}$, the fitting procedure clearly indicated that at least two distinct decays were present in $g^{(1)}(K, t)$. While single exponential fits of $g^{(1)}$ data yielded high (statistically weighted) χ^2 typically ≥ 5 (another indication of the presence of more than a single appreciable component in the data), biexponential fitting markedly reduced χ^2 by ~ 75%. Specifying two exponentials in the fitting routine with starting values for the relative amplitudes of 0.7 for component 1 and 0.3 for component 2 and the ratio $\Gamma_2/\Gamma_1 = 2$ resulted in a rapidly converging and stable fit whereby χ^2 exhibited changes no greater than 10^{-7} in consecutive passes through the Marquardt algorithm. Results of the double exponential fits of $g^{(1)}(K, t)$ were completely insensitive to the initial guesses for the amplitudes and relaxation rates. Such an observation further provides confidence that a global minimum in χ^2 was reached in the fits. Three exponential fits of $g^{(1)}$ did not substantially improve the fit over that obtained from the biexponential analysis.

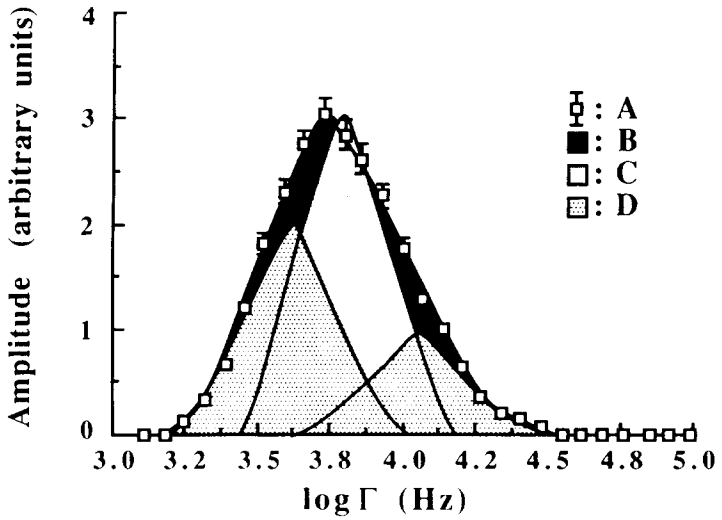

Figure A1. Results of Laplace inversion of the experimental and simulated correlation functions of M13mp19 ssDNA. (A) Derived from Laplace inversion of the experimentally obtained field correlation function, $g^{(1)}(K^2, t)$ at $\theta = 90°$ in 100 mM NaCl. The uncertainty level of the data is indicated by the error bars. (B) The distribution function obtained by inversion of the simulated biexponential function calculated from the relaxation rates, relative amplitudes, and superimposed random noise determined from fits of the experimental data. Note the close agreement of (B) with (A). (C) Obtained from inversion of a single exponential calculated from the relaxation rate, relative amplitude, and superimposed random noise determined from force fitting the experimental data with a single exponential function. (D) Obtained by inverting (separately) two simulated single exponential functions. The functions were calculated from the relaxation rates, relative amplitudes, and superimposed random noise of each component evaluated from a biexponential analysis of the experimental data.

This was generally the case in the four NaCl environments at all scattering angles.

To support the contention that a decaying biexponential with relaxation rates $\Gamma_1(K)$ and $\Gamma_2(K)$ and relative amplitudes $a_1(K)$ and $a_2(K)$ is indeed the best representation of $g^{(1)}(K, t)$, biexponential functions with different levels of background noise superimposed on them were calculated. These correlation functions were calculated using the relaxation rates Γ_1 and Γ_2 and amplitudes a_1 and a_2 evaluated from biexponential fits of the experimental data, and subected to exponential refitting. The noise was randomly generated at different levels with respect to the actual experimental noise level (determined from the standard deviation in the fits of the baseline, B_e). At a noise level equivalent to that present in the experimental data, nonlinear least squares biexponential fits of the simulated $g^{(1)}(K, t)$'s yielded relaxation rates and relative amplitudes identical to those obtained from the experimental data. Although not terribly surprising, such agreement is consistent with biexponential character (above the noise level) of our experimental $g^{(1)}(K, t)$.

Laplace Inversion of the Data

Laplace inversion of $g^{(1)}(K, t)$ [Eq. (A4)] measured in 100 mM NaCl at 90° and the simulated biexponential functions mentioned above were performed using the Laplace inversion routine EXSAMP.[73] A summary of the results of the analysis is depicted in Fig. A1. The curves in Fig. A1 clearly show the distribution function of the relaxation rates obtained by inversion of the actual experimental $g^{(1)}$ at 90° (A), and biexponential functions simulated with the relaxation rates, relative amplitudes, and superimposed noise determined from the biexponential fit of $g^{(1)}$ at 90° (B) are essentially identical within experimental error. In either case a single-peaked, fairly broad, and asymmetric distribution function is obtained [Fig. A1(A and B)]. The Γ distribution function obtained by inverting a single exponential function, calculated from the relaxation rate and amplitude evaluated from a nonlinear least squares fit of $g^{(1)}$ at 90° with a single exponential, also shows a single peak [Fig. A1(C)]. This peak, however, poorly represents the Γ distribution function obtained from the actual data and clearly indicates deviations of the actual data from single exponential behavior. These observations do not contradict our basic contention; the correlation functions measured on M13mp19 circular ssDNA are best represented as a biexponential.

We are grateful to Professor Paul Russo of the Chemistry Department at Louisiana State University for generously providing the invaluable data transfer and analysis software. We thank Professor P. R. LeBreton for his cooperation, Professor P. R. Young for his continual interest in these studies, and Mitchel Doktycz for careful reading of the manuscript. This work was supported in part by NIH grant GM39471, an Institutional Research Grant from the American Cancer Society, and a grant from the Campus Research Board of the University of Illinois at Chicago.

REFERENCES

1. Coleman, J. E. & Oakley, J. L. (1980) *CRC Crit. Rev. Biochem.* **7**, 247–289.
2. Kowalczykowski, S. C., Bear, D. G. & von Hippel, P. H. (1981) *Enzymes* **14**, 373–444.
3. Marians, K. J. (1984) *CRC Crit. Rev. Biochem.* **17**(2), 153–215.
4. Wickner, S. H. (1978) *Ann. Rev. Biochem.* **47**, 1163–1191.
5. Kahn, R. & Radding, C. M. (1984) *J. Biol. Chem.* **259**, 7495–7503.
6. Kodadek, T. & Alberts, B. M. (1987) *Nature* **326**, 312–314.
7. Howard-Flanders, P., West, S. C. & Stasiak, A. (1984) *Nature* (London) **309**, 215–219.
8. Chase, J. W. & Williams, K. R. (1986) *Ann. Rev. Biochem.* **55**, 103–136.
9. van Amerongen, H., van Grondelle, R. & van der Vliet, P. C. (1987) *Biochemistry* **26**, 4646–4652.
10. Romer, R., Schomburg, U., Krauss, G. & Maass, G. (1984) *Biochemistry* **23**, 6132–6137.
11. Khamis, M. I., Casas-Finet, J. R., Maki, A. H., Murphy, J. B. & Chase, J. W. (1987) *J. Biol. Chem.* **262**(23), 10938–10945.
12. Shimamoto, N. & Utiyama, H. (1983) *Biochemistry* **22**, 5869–5878.
13. Lohman, T. M., Overman, L. B. & Datta, S. (1986) *J. Mol. Biol.* **187**, 603–615.
14. Boidot-Forget, M., Saison-Behmoaras, T. Toulmé, J.-J. & Helene, C. (1986) *Biochemie* **68**, 1129–1134.
15. Overman, L. B., Wlodzimierz, B. & Lohman, T. M. (1988) *Biochemistry* **27**, 456–471.
16. Prasad, B. V. V. & Chiu, W. (1987) *J. Mol. Biol.* **193**, 579–584.
17. McPherson, A. & Brayer, G. D. (1985) in *Biological Macromolecules and Assemblies*, Vol. 2, Jurnak, F. A. & McPherson, A., Eds., John Wiley & Sons, New York, pp. 325–392.
18. Helene, C. & Maurizot, J. C. (1981) *Crit. Rev. Biochem.* **8**, 213–258.
19. Forsheit, A. B. & Ray, D. S. (1970) *Proc. Natl. Acad. Sci. USA* **67**(3), 1534–1541.
20. Halsall, H. B. & Schumaker, V. N. (1972) *Biochemistry* **11**, 4692–4695.

21. Newman, J., Swinney, H. L., Berkowitz, S. A. & Day, L. A. (1974) *Biochemistry* **13**, 4832–4838.
22. Chun, P. W., Herschleb, W. P., Downing, D. J. & Krista, M. L. (1974) *Biophys. Chem.* **1**, 141–151.
23. Edlind, T. D. & Ihler, G. M. (1980) *J. Mol. Biol.* **142**, 131–144.
24. Shen, J. C.-K., Ikoku, A. & Hearst, J. E. (1979) *J. Mol. Biol.* **127**, 163–175.
25. Shen, J. C.-K. & Hearst, J. E. (1979) *Anal. Biochem.* **95**, 108–116.
26. Blakesley, R. W. & Wells, R. D. (1975) *Nature* (London) **257**, 421–422.
27. Reckmann, B., Grosse, F., Urbanke, C., Frank, R., Blocker, H. & Krauss, G. (1985) *Eur. J. Biochem.* **152**, 633–643.
28. Leahy, M. C. & Radding, C. M. (1986) *J. Biol. Chem.* **261**, 6954–6960.
29. Flory, S. S., Tsang, J., Muniyappa, K., Bianchi, M., Gonda, D., Kahn, R., Azhderian, E., Egner, C., Shaner, S. & Radding, C. M. (1984) *Cold Spring Harbor Symp. Quant. Biol.* **49**, 513–523.
30. Kowalczykowski, S. C., Clow, J., Somani, R. & Varghese, A. (1987) *J. Mol. Biol.* **193**, 81–95.
31. van de Sande, J. H., Ramsing, N. B., Germann, M. W., Elhorst, W., Kalisch, B. W., Kitzing, E. V., Pon, R. T., Clegg, R. C. & Jovin, T. M. (1988) *Science* **241**, 551–557.
32. Ramsing, N. B. & Jovin, T. M. (1988) *Nucleic Acids Res.* **16**, 6659–6676.
33. Germann, M. W., Kalisch, B. W. & van de Sande, J. H. (1988) *Biochemistry* **27**, 8302–8306.
34. Rouse, P. E. (1953) *J. Chem. Phys.* **21**, 1272–1280.
35. Zimm, B. H. (1956) *J. Chem. Phys.* **24**, 269–278.
36. Lin, S.-C. & Schurr, J. M. (1978) *Biopolymers* **17**, 425–461.
37. Thomas, J. C., Allison, S. A., Schurr, J. M. & Holder, R. D. (1980) *Biopolymers* **19**, 1451–1474.
38. Norrander, J., Kempe, T. & Messing, J. (1983) *Gene* **26**, 101–106.
39. Maniatis, T., Fritsch, E. F. & Sambrook, J. (1982) *Molecular Cloning*, Cold Spring Harbor, New York, pp. 249–251.
40. Messing, J., Crea, R. & Seeburg, P. H. (1981) *Nucleic Acids Res.* **9**, 309–321.
41. Yamamoto, K. R. & Alberts, B. M. (1970) *Virology* **40**, 734–744.
42. Been, M. D. & Champoux, J. J. (1983) *Methods Enzymol.* **101**, 90–98.
43. Pohl, F. & Jovin, T. (1972) *J. Mol. Biol.* **67**, 375–396.
44. Berne, B. J. & Pecora, R. (1976) *Dynamic Light Scattering*, John Wiley & Sons, New York, p. 26.
45. Thomas, J. C. & Schurr, J. M. (1979) *Opt. Lett.* **4**, 222–223.
46. Utiyama, H. (1972) in *Light Scattering from Polymer Solutions*, Huglin, M. B., Ed., Academic Press, New York, pp. 61–88.
47. Young, P. R., Vacante, D. A. & Synder, W. R. (1982) *J. Am. Chem. Soc.* **104**, 7287–7291.
48. Tanford, C. (1961) *Physical Chemistry of Macromolecules*, John Wiley & Sons, New York, pp. 298–313.
49. Stokes, R. H. & Mills, R. (1965) in *The International Encyclopedia of Physical Chemistry and Chemical Physics*, Topic 16, Vol. 3, Stokes, R. H., Ed., Pergamon Press, New York, p. 118.
50. Langowski, J. (1987) *Biophys. Chem.* **27**, 263–271.
51. Wilcoxon, J. & Schurr, J. M. (1983) *Biopolymers* **22**, 2273–2321.
52. Schurr, J. M. (1977) *CRC Crit. Rev. Biochem.* **4**, 371–431.
53. Wartell, R. M. & Benight, A. S. (1985) *Phys. Rep.* **126**, 69–107.
54. Oster, G. (1948) *Chem. Rev.* **43**, 319–365.
55. Shibata, J. H. & Schurr, J. M. (1981) *Biopolymers* **20**, 525–549.
56. Bloomfield, V. A. (1985) in *Dynamic Light Scattering, Applications of Photon Correlation Spectroscopy*, Pecora, R., Ed., Plenum Press, New York, p. 386.
57. Spetter, S., Chen, C., Warren, R. A. J. & Hanlon, S. (1985) *Biochim. Biophys. Acta* **838**, 312–320.
58. Gray, D. M., Edmonson, S. P., Lang, D. & Vaughn, M. (1979) *Nucleic Acids Res.* **6**, 2089–2106.
59. Steely, H. T., Jr., Gray, D. M. & Ratliff, R. L. (1986) *Nucleic Acids Res.* **14**, 10071–10090.
60. Lin, S.-C., Thomas, J. C., Allison, S. A. & Schurr, J. M. (1981) *Biopolymers* **20**, 209–230.
61. Caloin, M., Wilhelm, B. & Daune, M. (1977) *Biopolymers* **16**, 2091–2104.
62. Schmitz, K. S. (1979) *Biopolymers* **18**, 479–484.
63. Bloomfield, V. A., Crothers, D. M. & Tinoco, I., Jr. (1974) *Physical Chemistry of Nucleic Acids*, Harper & Row, New York.
64. Cantor, C. R. & Schimmel, P. R. (1980) *Biophysical Chemistry*, part II, W. H. Freeman & Company, New York, pp. 409–432.
65. Hagerman, P. J. (1988) *Ann. Rev. Biophys. Biophys. Chem.* **17**, 265–286.
66. Eisenberg, H. (1987) *Acc. Chem. Res.* **20**, 276–282.
67. Schurr, J. M. & Schmitz, K. S. (1986) *Ann. Rev. Phys. Chem.* **37**, 271–305.
68. Inners, L. D. & Felsenfeld, G. (1970) *J. Mol. Biol.* **50**, 373–389.
69. Koppel, D. E. (1972) *J. Am. Chem. Soc.* **57**, 4814–4820.
70. Bevington, P. R. (1969) *Data Reduction and Error Analysis for the Physical Sciences*, McGraw Hill, New York.
71. Ford, N. C., Jr. (1985) in *Dynamic Light Scattering, Applications of Photon Correlation Spectroscopy*, Pecora, R., Ed., Plenum Press, New York, p. 18.
72. Jakeman, E., Oliver, C. J. & Pike, E. R. (1970) *J. Phys. A* **3**, L45–L48.
73. Bertero, M., Brianzi, P., Pike, E. R., deVillers, G., Lan, K. H. & Ostrowsky, N. (1985) *J. Chem. Phys.* **82**, 1551–1554.

Received August 10, 1988
Accepted February 10, 1989